Hole drift mobility measurements in polycrystalline $CuIn_{1-x}Ga_xSe_2$

S. A. Dinca and E. A. Schiff
Department of Physics, Syracuse University, Syracuse, New York 13244-1130, USA

B. Egaas, R. Noufi, and D. L. Young
National Renewable Energy Laboratory, Golden, Colorado 80401, USA

W. N. Shafarman
Institute of Energy Conversion, University of Delaware, Newark, Delaware 19716, USA

(Received 21 July 2008; revised manuscript received 22 July 2009; published 2 December 2009)

We present temperature-dependent hole drift mobility measurements on polycrystalline $CuIn_{1-x}Ga_xSe_2$ (CIGS) thin films incorporated into solar-cell structures. The drift mobilities were determined from photocarrier time-of-flight measurements in a depletion region at the top interface with cadmium sulfide. 12 cells, originating in two laboratories, were examined. The drift mobilities ranged from 0.02 to 0.7 cm^2/Vs at room temperature and were weakly temperature dependent in the range of 100–300 K. These drift mobilities are at the low end of the range of hole mobilities reported from previous Hall effect and admittance measurements for varying CIGS materials. We found approximately a square-root correlation between the width of the depletion layer in our samples and the magnitude of the drift mobility. Both the magnitude and the temperature dependence of the drift mobility are consistent with results in amorphous and nanocrystalline silicon that have been modeled using a disorder-induced transport edge. The source of nanometer-scale disorder in these CIGS materials is not noncrystallinity; chemical composition fluctuations are one alternative source of disorder. The correlation of the depletion-width and drift mobility measurements in CIGS may be evidence for a broader effect of disorder in these materials in both reducing the carrier drift mobility and generating acceptor defects near the valence bandedge. Hole drift mobilities are sensitive to disorder-induced traps near the valence bandedge. Our temperature-dependence measurements indicate that the width of the corresponding valence bandtail is less than 20 meV. Previous optical-absorption spectroscopy showed that Urbach tails in similar CIGS samples are generally 20 meV or wider, which indicates that the valence bandtail does not typically determine the Urbach tails.

DOI: 10.1103/PhysRevB.80.235201 PACS number(s): 72.80.Ng, 72.40.+w, 72.20.Jv

I. INTRODUCTION

Despite grain boundaries and other defects, polycrystalline copper indium diselenide ($CuInSe_2$) and the related polycrystalline quaternary alloy $CuIn_{1-x}Ga_xSe_2$ (CIGS) have very good electronic properties compared to their more ordered, crystalline counterparts. One striking illustration of these properties is that solar cells fabricated from the thin-film polycrystalline materials have larger conversion efficiencies—approaching 20%—than the cells prepared from the single-crystal materials.[1–3]

This counterintuitive, and fortuitous, effect reveals the limitations of our present understanding of CIGS and other semiconductors in their more disorderly forms. The grain boundaries have naturally attracted a good deal of attention, and there have been several recent experimental and theoretical papers that elaborate the grain-boundary properties and that explore possible theories for them.[4,5] In addition to the grain boundaries, the properties of the crystallites within the materials differ from those of relatively perfect single crystals. Since both effects are potentially significant, it is important to determine which effect is dominant in a given material and for a given material property.

One important property that varies substantially between the different forms of CIGS is the hole mobility. Hole mobilities inferred from the Hall effect in single crystals,[6–10] can be as large as 10^3 cm^2/Vs, whereas Hall mobilities of 1 cm^2/Vs and lower have been reported for some polycrystalline materials.[11–19] Some of these measurements are presented in Fig. 1 (solid curves). In the present paper, we present hole mobilities in polycrystalline CIGS obtained using the photocarrier time-of-flight (TOF) technique.[20] The method itself is well established, and involves measuring the transit times of carriers that are photogenerated near one electrode and then drift across a layer in an electric field.

TOF mobility measurements complement the Hall-effect measurements. In single crystals, Hall mobilities are indicative of fundamental band mobilities, whereas time-of-flight measures drift mobilities; drift mobilities can be smaller than band mobilities because they are sensitive to shallow traps that capture and release carriers during their transit.[20] In polycrystalline and amorphous materials, the Hall effect no longer yields a band mobility directly. In polycrystalline materials the Hall effect has been modeled by invoking electrostatic barriers between grains;[21] in amorphous materials, even the sign of the Hall voltage is poorly understood.[22,23] The interpretation of time-of-flight measurements in terms of drift mobilities still applies in the disordered systems and modeling must again be used to distinguish band transport and trapping effects.[20,24]

As is illustrated in Fig. 1, the range of drift mobilities (0.02–0.7 cm^2/Vs) that we have found using TOF in samples of polycrystalline CIGS is somewhat lower than the range of mobilities using other techniques. Our samples

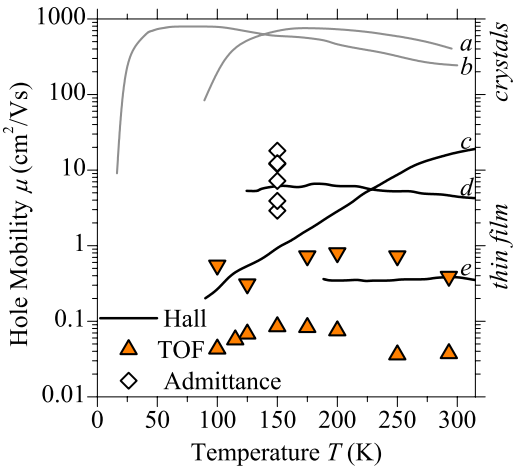

FIG. 1. (Color online) Temperature-dependent hole mobilities reported for $CuIn_xGa_{1-x}Se_2$. The solid curves are Hall-effect measurements (a): $x=1$ (Ref. 6), (b): $x=0.031$ (Ref. 6), (c): $x=1$ (Ref. 11), [(d) and (e)]: $x=1$ (Ref. 14). (a) and (b) are for single crystals; all other measurements are done on thin-film polycrystalline samples. The admittance measurements correspond to $x=0.00-0.34$ (Ref. 58). TOF measurements are from the present work ($x=0.3$).

came from the National Renewable Energy Laboratory (NREL) and from the Institute of Energy Conversion (IEC). The hole drift mobilities were generally smaller in the NREL samples than the IEC samples. We found a correlation across both series of samples between the drift mobilities and the widths of the depletion layers. In Fig. 2 we have plotted the depletion widths (at 0 V) for the varying drift mobilities on logarithmic scales; there is approximately a square-root dependence. Since the depletion width in *p*-type samples is roughly proportional to the reciprocal square root of the acceptor density, the correlation suggests that a single underlying mechanism determines both the drift mobility and the acceptor density.

In the time-of-flight measurements the photocarriers do not typically traverse grain boundaries and it thus seems unlikely that grain boundaries control the drift mobilities. The

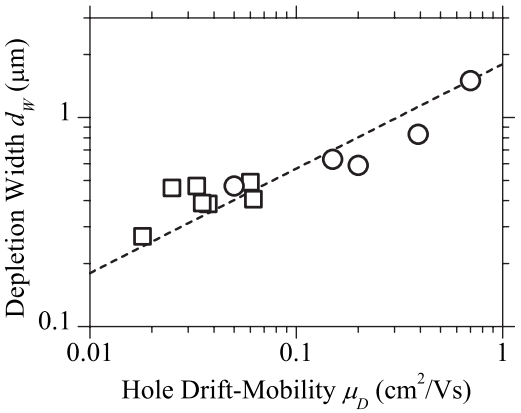

FIG. 2. Correlation of the depletion width (at 0 V) and the hole drift mobility for twelve CIGS samples at room temperature. The dashed line indicates square-root dependence. □—NREL samples. ○—IEC samples.

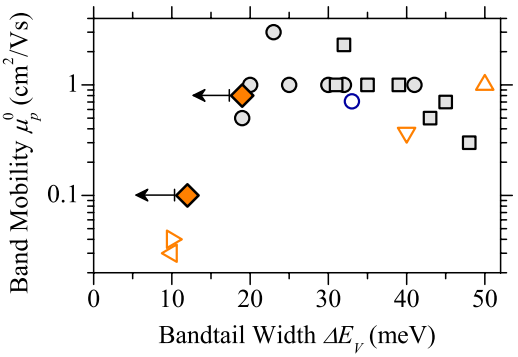

FIG. 3. (Color online) Correlation of estimates for the effective-band mobility and the bandtail width for several disordered materials. ♦—CIGS (this work). ○—PbI_2 (Ref. 37). ◁—sexithiophene (Ref. 34). ▷—dihexyl-sexithiophene (Ref. 34). △—regioregularpoly(thiophene) (Ref. 35). ▽—pentacene (Ref. 36). Gray symbols: a-Si:H, a-SiGe:H, and nc-Si:H (Ref. 24).

correlation that we report between the depletion width and the drift mobilities is suggestive of ionized impurity scattering as the mobility-limiting mechanism.[25] However, the present polycrystalline samples have mobilities smaller by about 1000 times than the single crystals to which this mechanism has been applied;[9,26–28] previous workers have also discarded this mechanism as descriptive of polycrystalline CGS.[28] We think that the magnitude and the temperature dependence are suggestive of mobilities for electronic states close to a "mobility edge," which is the electronic energy near the bandedge that separates states that are localized by disorder from states that remain extended. Disordered silicons, either amorphous or nanocrystalline, are probably the best studied materials with transport ascribed to a mobility edge.[24–30] For thin-film CIGS, where the crystallite sizes are much larger than in the nanocrystalline silicon materials, nanometer-scale chemical composition fluctuations reported previously[31] may be the source of disorder creating a mobility edge. This idea was previously considered (and discarded) for InGaAsN.[32]

A typical depletion width in our samples is 0.3 μm, which corresponds to an acceptor density of order 10^{16} cm^{-3} and a typical separation between acceptors of about 50 nm. As we discuss subsequently, this is much longer than the mean-free path that corresponds to our mobilities. We speculate that the correlation of the drift mobility with the depletion width occurs because both the mobility and the acceptor density are determined by the underlying disorder within individual crystallites of CIGS, which also implies that the acceptor sites correspond to regions in CIGS crystallites with much larger than typical chemical disorder.[33]

Disordered materials typically have both low band mobilities and bandtails of localized states near their bandedges. Temperature-dependent drift mobility measurements have been used extensively to estimate the bandtail widths. In Fig. 3 we present a plot of the band mobilities and bandtail widths that have been reported in some organic and polymeric materials,[34–36] in PbI_2,[37] in disordered silicons,[24] and in our present work on CIGS. From our modeling of the CIGS measurements, we are only able to report upper limits

TABLE I. Summary of the structural compositions and the photovoltaic parameters of the specimens of $CuIn_{1-x}Cu_xSe_2$ at 293 K. The symbol definitions are as follow: E_g is the band gap, V_{OC} is the open-circuit voltage, J_{sc} is the short circuit current, FF is the field factor (AM 1.5 illumination conditions), d is the geometrical thickness of the CIGS absorber layer, d_W is the depletion width of the CIGS absorber layer (this property was estimated from capacitance measurements at 0 V), μ_D is the hole drift mobility, and $\mu\tau$ is the hole deep-trapping mobility-lifetime product (these properties were obtained from the transient photocurrent measurements).

Sample	IEC-1	IEC-2	IEC-3	NREL-1	NREL-2
Cu/[In+Ga]	0.82	0.82	0.79	~0.88	~0.88
Ga/[In+Ga]=x	0.30	0.30	0.25	~0.30	~0.30
E_g(eV)	1.18	1.18	1.12	~1.15	~1.15
V_{OC}(V)	0.616	0.636	0615	0.626	0.690
J_{SC}(mA/cm^2)	33.4	32.2	30.4	30.9	31.2
FF	72.9	76.1	74.1	68.9	77.2
Efficiency (%)	15	15.6	13.9	13.3	16.6
d(μm)	2	2	2.3	2.6	~2.5
d_W(μm) (0 V)	0.6	0.85–1.1	0.5–1.5	0.4–0.5	0.3–0.5
μ_D(cm^2/Vs)	0.15	0.4	0.05–0.7	0.03–0.06	0.02–0.06
$\mu\tau$(10^{-7} cm^2/Vs)	0.11	0.4	0.3–1.2	0.5–6.0	0.2–0.75

for the valence bandtail widths; nonetheless, our measurements on CIGS are broadly comparable to those in other disordered materials.

The limits on bandtail widths are interesting in the context of optical-absorption coefficient spectra of CIGS materials, which exhibit "Urbach tails" with their own characteristic energy widths E_U. The bandtail width is one component of the Urbach tail but most CIGS materials have Urbach energies that are larger than our limiting values near 20 meV.[38–44] We presume that the different types of disorder (composition fluctuations, structural defects, and electric field fluctuations) affect the Urbach energy and the valence bandtail width differently.

In the remainder of the paper we present our experimental measurements and a more detailed discussion of their interpretation and significance. Time-of-flight measurements are usually done in highly insulating materials with negligible space charge. The CIGS cells we studied have a depletion layer in the upper region where photogeneration occurs and we needed to modify the conventional time-of-flight procedures to take the depletion layer into account. As noted previously, there is a fairly strong correlation between the magnitude of the drift mobility and the width of the depletion layer. We also compare the temperature dependence of our measurements with the predictions of a well-known bandtail trapping model although our measurements are inconclusive regarding its validity for CIGS.

II. SPECIMENS

The $CuIn_{1-x}Ga_xSe_2$ thin-film solar cells used for the present measurements were prepared at the NREL and at the Institute of IEC at the University of Delaware.

The CIGS absorbers provided by NREL have been grown on Mo-coated soda-lime glass by evaporation from elemental sources following the "three-stage"[1,45] process developed at NREL. The Mo layer has a thickness of around 1 μm and is deposited by dc magnetron sputtering. The ~2.6-μm-thick $CuIn_{1-x}Ga_xSe_2$ absorbers incorporate a slight modification in the Ga content and substrate heating profile. Essentially, the Ga content in the first stage (~30% relative to In) is higher than that of the third stage (~25% relative to In). A cadmium sulfide (CdS) buffer layer is deposited next using chemical-bath deposition (CBD). Finally, a zinc oxide (ZnO) window layer is deposited using sputtering. The ~50-nm-thick insulating ZnO is grown from an intrinsic ZnO target, whereas the ~350-nm-thick conductive layer comes from an Al_2O_3-doped ZnO target (2 wt %).

The cells from IEC have the following configuration: glass/Mo/$CuIn_{1-x}Ga_xSe_2$/CdS/ZnO/indium tin oxide (ITO)/(Ni/Al grid). The CIGS thin films were grown using elemental thermal evaporation[46,47] (four source elemental evaporation) on top of a 0.7-μm-thick sputtered Mo layer. The CdS was deposited by CBD and has a nominal thickness of 40 nm. The last two layers ZnO and ITO where both deposited using the RF sputtering deposition. The resulting layers have a nominal thickness of 50 nm for ZnO, respectively, 0.2 μm for ITO. Finally, electron-beam evaporation was used to deposit Ni/Al grids. The specimen areas were determined by mechanical scribing in order to define an active region.

The alloy compositions and photovoltaic parameters of the specimens used in this research are given in Table I. The composition ratios were obtained from electron probe microanalysis. The photovoltaic parameters of the cells are measured under standard conditions: 1000 W/cm^2, 25 °C, ASTM E 892 Global. The band-gap values are estimated from the internal quantum efficiency measurements[1] for NREL specimens, and inferred from the compositional[46] variation for the IEC specimens.

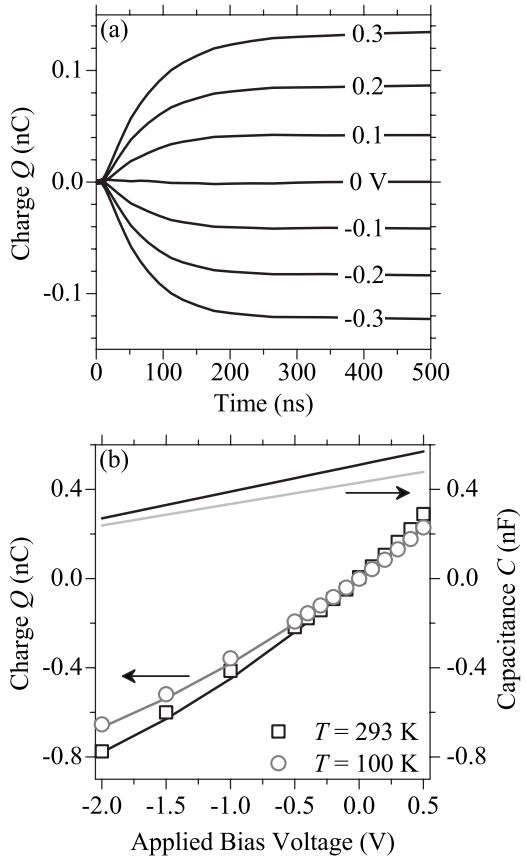

FIG. 4. (a) The transient charge $Q(t)$ measured following application of a bias voltage step (indicated) at room temperature. (b) The open symbols indicate the charge response Q at 300 ns after the step. The line through these data is a quadratic fit through the origin. The capacitance (dashed line) was calculated using the charge fitting parameters (NREL-2, 293 and 100 K, electrode area is 1.32×10^{-2} cm^2).

III. CAPACITANCE AND DEPLETION-WIDTH MEASUREMENTS

The CIGS cells that we studied have depletion layers[48] near the top interface (CIGS/CdS), which is consistent with previous work on similar CIGS cells. Depletion layers correspond to nonuniform electric fields across the sample and they complicate time-of-flight measurements, which are typically done under conditions of near-uniform fields.[20] Perhaps the most significant complication is that the effective thickness of the sample that is used in calculating the mobility from the photocarrier "transit time" is the depletion width, which is usually substantially smaller than the physical thickness of the CIGS layer.

As part of a time-of-flight measurement, most practitioners do a somewhat unconventional large-signal capacitance measurement. We apply a voltage step to the sample using a pulse generator; the current flowing onto the sample electrodes was computed from the response of a preamplifier as recorded by a digital oscilloscope. This transient current was numerically integrated to obtain the transient charge. Figure 4(a) illustrates the charge-transient measurements. As can be seen, the charge reaches a plateau at about 300 ns. At longer times there is also an increase in charge due mostly to resistive currents through the device; these can be probed using the charge recovery when the voltage returns to zero but we do not discuss this aspect further in this paper.

Figure 4(b) is a plot of the charge measurements for the CIGS cell evaluated at 300 ns following the voltage step. As can be seen, there is a moderate nonlinearity of the Q-V relation. A simple quadratic fitting $Q=aV+bV^2$ worked reasonably well, and we determined the fitting parameters a and b for all cells, voltages, and temperatures we studied. We calculate a capacitance using $C=\frac{dQ}{dV}=a+2bV$, which is also illustrated in Fig. 4(b).

We define the corresponding depletion width as $d_W=\frac{\varepsilon_r\varepsilon_0 A}{C}$, where A is the area of the cell and $\varepsilon_r\varepsilon_0$ is the dielectric constant of CIGS. We were able to determine the relative dielectric constant[49] $\varepsilon_r=Cd/\varepsilon_0 A$ of the CIGS absorber layers for some of the IEC cells that had weak depletion at lower temperatures. The geometrical thickness $d=2.0$ μm of the thin film had been measured during film growth using a quartz-crystal monitor; the capacitance, $C=4.2\times10^{-11}\pm0.1\times10^{-11}$ F did not vary noticeably with temperature over the range 100–175 K; at higher temperatures depletion effects noticeably affected the capacitance and precluded using the method. We obtained the dielectric constant $\varepsilon_r=11.8\pm0.3$, which is consistent with the value used with admittance measurements[58] on similar CIGS materials.

Using this value for ε_r, for the particular sample in Fig. 4(b) $d_W=270$ nm at 0 V applied bias (293 K). This value is substantially less than the thickness 2500 nm of the CIGS layer (from Table I). This fact, as well as the fact that the capacitance decreases under reverse bias, are broadly consistent with depletion widths. We note that the textbook Schottky model $(A/C)^2=2(V_{BI}-V)/(N_A e\varepsilon_r\varepsilon_0)$ is not a good description of the measurements. We return to the subject of the field profile in the depletion region in the Appendix A.

IV. TIME-OF-FLIGHT PROCEDURES

Time-of-flight measures the transit time t_T required to move the mean position of the photocharge charge distribution a length L under the influence of the bias voltage V. TOF measurements were done using a nitrogen-laser pumped dye laser with a 3 ns pulse. The cells were illuminated through the top, n-type CdS buffer layer. The laser wavelength was typically 700 nm. The absorption coefficient α in CIGS ($x=0.3$) at this wavelength is about $\alpha=8\times10^4$ cm^{-1}.[50,51] The reciprocal of this absorption coefficient gives an absorption depth of about 120 nm. For time-of-flight measurements one usually arranges for this length to be significantly smaller than the appropriate thickness, which was the depletion width in our case. As is evident from Table I, the absorption length is not completely negligible, but we did not correct for its finite magnitude in our analysis.

A pulsed bias voltage was applied across the cells 1.0 μs prior to the arrival of the laser pulse. This time delay was chosen based on measurements such as those in Fig. 4, which indicate that dielectric relaxation within the sample was essentially complete on that time scale. The usual reason

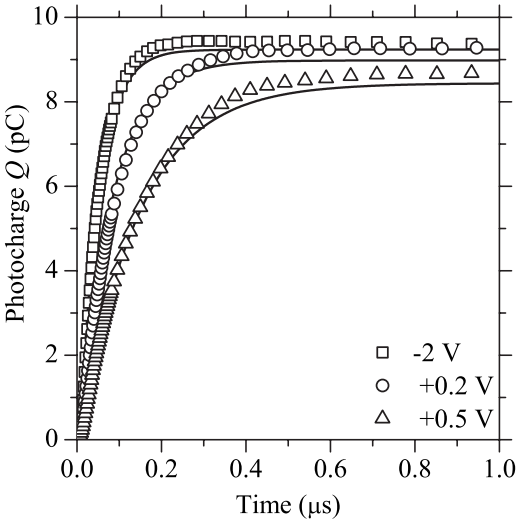

FIG. 5. Transient photocharge magnitude $|Q(t)|$ at varying bias voltages $(-2.0, +0.2, +0.5)$. The curves are a fitting to the entire family of measurements using the modified Hecht Eq. (1). (NREL-2, 293 K, $A = 1.32 \times 10^{-2}$ cm^2).

for using pulsed bias in time-of-flight measurements is to measure the transit time prior to significant dielectric relaxation, in which case most workers assume a constant uniform electric field. This procedure was not workable in these CIGS samples. In our case, we used pulsed bias so that we could both monitor the electric field evolution (currents prior to the laser pulse) and then the photocarrier motion (by monitoring the photocurrent).

The photocurrent and photocharge transients were measured using the same apparatus described in Sec. III; the transients were typically averaged over 100 laser shots to improve the signal-to-noise ratio. Specimens were mounted on the cold finger of a commercial vacuum cryostat (Oxford instruments model DN 1754).

The laser intensity was attenuated by neutral density filters so that the photocarrier charge collected in the external circuit was 10% or less of the bias charge on the sample electrodes as measured in the capacitance experiments. This precaution is intended to assure that the photocharge generated by the laser does not significantly perturb the electric field profile in the cell. The repetition rate of the laser was reduced until the transient photocurrent was independent of the repetition rate; a 1 Hz repetition rate was adequate.

In Fig. 5, the symbols indicate the measurements of the absolute value of the transient photocharge $|Q(t)|$ for three applied voltages V; measurements were also made for several intermediate voltages but are not shown. As can be observed, the photocharge $|Q(t)|$ has generally reached a plateau by 1000 ns. It is also evident that the rise time (the time to reach 50% of the ultimate photocharge) lengthens substantially as the bias voltage changes from −2.0 to +0.5 V. This voltage span corresponds to decreasing magnitude of the net voltage V_{BI}-V across the depletion layer; the increase in the risetime for decreasing magnitude is typical of time-of-flight measurements. The smooth curves are a fitting to the entire family of measurements, including several voltages that are not illustrated. We now discuss this fitting.

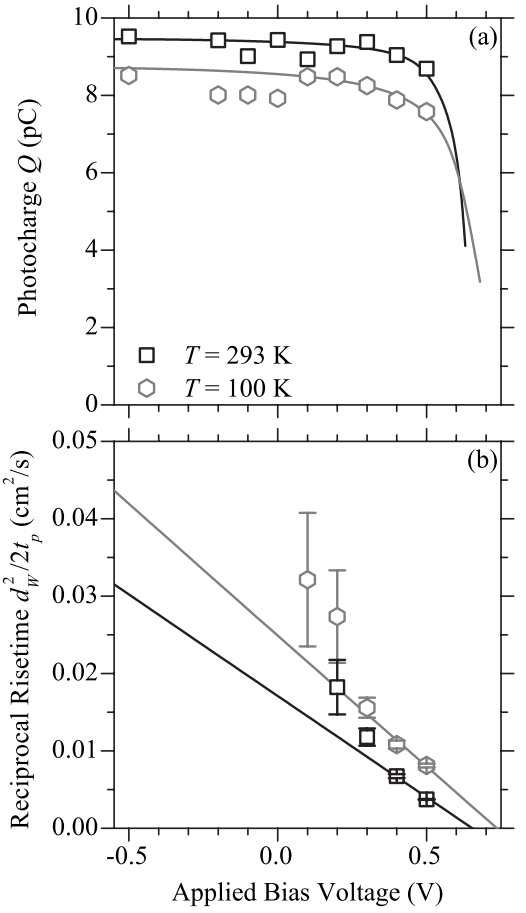

FIG. 6. The symbols indicate (a) photocharge measured at 1000 ns and (b) photocharge risetime measurements for varying bias voltages on sample NREL-2; results for two temperatures are indicated. The solid lines are fittings using the modified Hecht expression (293 K: $\mu_D = 0.018$ cm^2/Vs, $\mu\tau = 2 \times 10^{-8}$ cm^2/V, and $V_{BI} = 0.64$ V; and 100 K: $\mu_D = 0.02$ cm^2/Vs, $\mu\tau = 1 \times 10^{-8}$ cm^2/V, and $V_{BI} = 0.7$ V).

In the simplest examples of photocarrier time-of-flight experiments, the plateau photocharge is voltage independent and may be identified with the total photocharge Q_0 absorbed by the sample; the only effect of changing the bias voltage is to change the transit time for a carrier to cross the sample. For this CIGS cell, the photocharge is slightly voltage dependent, as is further illustrated in Fig. 6(a) at two temperatures. Failure to collect all the photocharge for smaller net voltages V_{BI}-V is fairly common in time-of-flight measurements. It is usually attributed to "deep trapping," which is the capture of holes by defect levels that do not reemit them on the scale of the transit time.[52,53]

Deep trapping is characterized by a mobility-lifetime product $\mu\tau$. We assume for the moment that μ is the band mobility of the holes and τ is their deep-trapping time. If the electric field were uniform, corresponding to a voltage-independent capacitance, we would apply a well-known fitting expression called the "Hecht" formula.[54,55] Our capacitance measurements depended significantly on voltage, which indicates a nonuniform electric field. As a better approximation, we modified the Hecht analysis to apply to

Schottky-type depletion layers; the derivation is in Appendix B. The corresponding form of the photocurrent transient is then

$$Q(t) = Q_0 \frac{\tau}{t_T + \tau}[1 - \exp(-t/t_T)\exp(-t/\tau)],$$

$$t_T \equiv \frac{d_W^2}{2\mu_D(V_{BI} - V)}, \tag{1}$$

where t_T is a transit time, d_W is the depletion width, and V_{BI} is the built-in potential across the depletion layer. The formulas for the asymptotic photocharge Q_∞ and for the photocharge risetime t_p (time to reach 50% of the asymptotic charge) are

$$Q_\infty(V) = Q_0\left[1 + \frac{d_W^2}{2\mu\tau(V_{BI} - V)}\right]^{-1}, \tag{2a}$$

$$\frac{d_W^2}{2t_p} = \left[\mu_D(V_{BI} - V) + \frac{d_W^2}{2\tau}\right]/\ln(2). \tag{2b}$$

Note that, for long deep-trapping times ($\tau \to \infty$), the formulas reduce to $Q_\infty = Q_0$ and $d_W^2/2t_p = \mu_D(V_{BI} - V)/\ln(2)$. Figure 6(b) presents the photocharge risetime measurements corresponding to the photocharge measurements in Fig. 6(a); we have corrected for the laser pulsewidth and the electronic risetime as explained in Appendix C. The risetime measurements are presented as the voltage dependence of $d_W^2/2t_p$, which is the form suggested by Eq. (2b). The error bars on each point in Fig. 6(b) were determined by making several risetime measurements at a given voltage and propagating the risetime error into the error in the ratio $d_W^2/2t_p$. The large errors for more negative bias voltages occur because the photocharge risetime approaches the shortest value permitted by the laser pulsewidth and the electronic response time.

In Figs. 5 and 6 we also show the fittings to Eqs. (1) and (2); the fitting parameters are given in the figure caption. As can be seen, the exponential form of Eq. (1) fits the form of the transient photocharge in Fig. 5 fairly well and Eqs. (2a) and (2b) account fairly well for the voltage dependence of the photocharge and of the risetime.

One important check of the fittings is the comparison of the built-in potential parameter V_{BI} with the open-circuit voltages of the samples under solar illumination at room temperature, which is $V_{OC} = 0.69$ V. The built-in potential estimate (0.64 V) is around V_{OC} as required by the simplest solar-cell analysis.[56] On the other hand, the reciprocal risetimes for the most negative voltages are somewhat larger than expected from the fitting. This may be related to our approximation, used in deriving Eq. (1) and (2) that the electric field falls linearly to zero from the interface; if this assumption were strictly true it would require that the capacitance have a Schottky form $1/C^2 \propto (V_{BI} - V)$ as a function of voltage. Most of our measurements could be adequately fitted using the approach of Figs. 5 and 6.

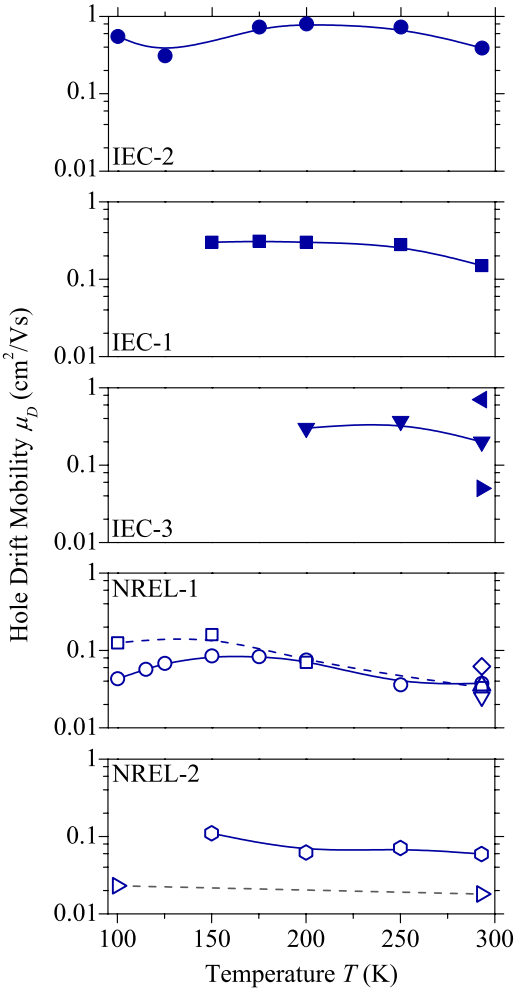

FIG. 7. (Color online) Hole drift mobilities μ_D for seven CIGS samples at varying temperature along with the room-temperature drift mobility of five other CIGS samples. The symbols indicates: IEC-1:■; IEC-2: ●; IEC-3: ▼, ▶, and ◀; NREL-1: □, ○, ◇, △, and ▽; and NREL-2: ⬡ and ▷.

V. SUMMARY OF MEASUREMENTS

In Fig. 7 we present the temperature-dependent drift mobilities for six samples. As can be seen, the drift mobility for most samples falls by a factor 2–3 from 150–300 K. One sample shows a distinct rise in the mobility from 100–150 K.

For each mobility estimate in Fig. 7 there are corresponding estimates of the mobility-lifetime product $\mu\tau$ and the built-in potential V_{BI}; we have reported the range of values for $\mu\tau$ at room temperature in Table I. One earlier experiment reported $\mu\tau = 6 \times 10^{-6}$ cm^2/V for holes in polycrystalline $CuGaSe_2$,[57] which is much larger than the range of our values. This presumably reflects a true materials difference.

In Fig. 1, we presented typical hole mobilities that have been reported for the CIGS system using three different techniques: Hall effect, admittance, and time of flight (present work). As noted earlier, Hall mobilities are not generally equivalent to drift mobilities; in addition, Hall measurements on CIGS use samples prepared on insulating substrates, whereas TOF samples (and solar cells) are prepared on metallic (typically Mo) substrates. Nonetheless, it appears from

Fig. 1 that the Hall effect may be a satisfactory indicator of drift mobilities in at least some CIGS thin films. The Hall mobilities reported on polycrystalline $CuGaSe_2$ thin films by Rusu *et al.*[14] [lines (d) and (e) in Fig. 1] have the small magnitude and weak temperature dependence that is characteristic of our drift mobilities. On the other hand, we found no evidence in the drift mobility measurements for a temperature dependence comparable to the hundredfold change in Hall mobility with temperature in polycrystalline $CuGaSe_2$ reported by Schuler *et al.*[12] [line (c) in Fig. 1]. The $CuGaSe_2$ films used in the two experiments are thought to differ in their stoichiometry $\frac{Ga}{Cu+Ga}$.

The mobilities that have been reported based on admittance measurements[58] are somewhat larger than we found in similar samples from the same laboratory (IEC). While the methods differ in detail, they are both drift mobility methods in the nanosecond domain. We think that the difference between the measurements may indicate that the hole mobility in these CIGS thin films is larger near the substrate interface than near the top interface to the CdS buffer. The admittance method is sensitive to transport processes in the undepleted, bottom region of the CIGS films while the TOF measurements probe the depleted zone near the top. We did find variability in mobilities from different diodes prepared on a single substrate and we also found a systematic overall difference between the mobilities in NREL and IEC samples. A change in mobility of a similar magnitude between the depletion region and the back of the films seems to be a plausible explanation for the difference in the admittance and the TOF measurements.

In Fig. 2, we presented the correlation we find between the depletion widths of the varying CIGS cells and the corresponding hole drift mobilities at room temperature; we found essentially the same correlation at 100 K.

VI. MOBILITY PERSPECTIVES: GRAIN BOUNDARIES, DISORDER SCATTERING, AND MOBILITY EDGES

Grain boundaries complicate the interpretation of electrical-transport measurements in polycrystalline materials and their effects are generally included in discussions of Hall mobilities. However, we think it unlikely that grain boundaries determine the CIGS drift mobilities of Fig. 1. First, the time-of-flight and admittance measurements involve carriers moving parallel to the growth axis of the thin films; since the films have crystallite sizes comparable to or larger than the film thickness, the measurements should mostly be sensitive to carrier motion within a single grain.[1] In addition, modeling and measurements of the Hall effect in polycrystalline silicon indicate that grain-boundary effects on transport are correlated with temperature dependence. Thus Seto found that grain boundaries in some polycrystalline silicon samples suppressed the Hall mobility well below the values in similarly doped single crystals.[21] The suppression was as large as 100 in one sample (see Fig. 2 in Ref. 21); for this sample, the Hall mobility had an activation energy of about 0.15 eV. Samples with smaller levels of grain-boundary suppression of the Hall mobility gave smaller activation energies. The drift mobilities we measured in our CIGS samples were not activated at higher temperatures and declined somewhat between 150 and 300 K.

We shall thus adopt the perspective that the drift mobility measurements on CIGS samples yielding the lower, weakly temperature-dependent mobilities of Fig. 1 are dominated by the properties of individual crystallites and are essentially equal to the mobility of carriers in electronic levels close to the valence-band edge. On the other hand, the larger magnitudes and stronger temperature dependence for the Hall mobilities of the samples studied by Schuler, *et al.*[12] that are also illustrated in Fig. 1 support their modeling that includes grain boundaries.

With this perspective, the low magnitude of the mobility in our CIGS samples reflects the disorder in these crystallites. Several types of disorder that reduce carrier mobilities have been studied in CIGS crystals and in CIGS thin films. For single crystals of $CuGaSe_2$, varying stoichiometries strongly affect the Hall mobility. These data are not illustrated in Fig. 1; at room temperature the Hall mobility range is from 60 to 300 cm^2/Vs, with a larger variation at lower temperatures.[59] Nanodomains of different elemental composition have been reported using electron microscopy both in CIGS single crystals and polycrystalline thin films.[31] Such nanodomains could be an alternative to point or line defects as the fundamental mechanism affecting mobilities in crystals.

Whatever the specific mechanism that lowers the mobilities by a 1000 fold or more below the values for well-ordered crystals, the mobilities are low enough that an effective-mass-based model for them is problematic. One way of seeing this is to compare the corresponding mean-free path l and the interatomic distance a; effective-mass theories are not generally applicable in systems with $l \leq a$, which is the "Ioffe-Regel" criterion.[23] We apply the expression $l=3\frac{kT}{e}\frac{\mu}{v_{th}}$ (v_{th} is the effective-mass thermal velocity and kT/e is the thermal voltage).[60] For a mobility of 1 cm^2/Vs and a thermal velocity $v_{th}=10^7$ cm/s, we obtain $l=0.075$ nm at room temperature, which is several times smaller than the interatomic distance.

We therefore suggest that the drift mobilities in our samples of polycrystalline CIGS are properties of a disorder-induced "transport edge." One possibility is that this edge is a mobility edge, which is the dividing line separating extended and localized states in the electronic density of states of a disordered material; while this edge should be sharp when it is close to the Fermi level, it is thought to be broadened somewhat by lifetime effects when it lies well above the Fermi level.[24,61] There are other transport models that give similar predictions for the band mobility;[23,61,62]; even pure hopping transport between localized bandtail states mimics the behavior of band transport models.[63–65] The present measurements on CIGS do not clearly distinguish between these mechanisms. Transport edges have frequently been associated with amorphous semiconductors, including at least some organic and polymeric materials, but they also describe carrier drift mobilities in some nanocrystalline silicon materials[24,66,67] and possibly in polycrystalline PbI_2 as well.[37] As indicated in Fig. 3, the band mobilities associated with these materials are typically around 0.1–1 cm^2/Vs,

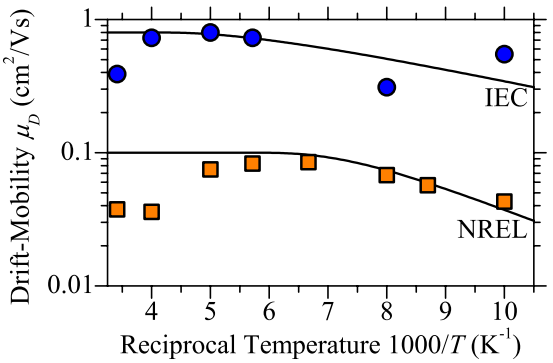

FIG. 8. (Color online) The symbols indicate temperature-dependent drift mobility measurements for two samples IEC-2 and NREL-1. The lines are calculations using the exponential bandtail multiple-trapping model. Both calculations use the emission prefactor frequency $\nu_0=10^9$ s^{-1}; we used $\mu_p^0=0.8$ cm^2/Vs and $\Delta E_V=19$ meV for the sample with the larger drift mobility, and $\mu_p^0=0.1$ cm^2/Vs and $\Delta E_V=12$ meV for the sample with the smaller mobility.

which agrees with the range of drift mobilities that we are reporting for CIGS.

In materials with disorder-induced transport edges, Hall mobilities are not well understood.[23] Amorphous semiconductors typically exhibit Hall-sign anomalies: the polarity of the Hall voltage is reversed from the predictions of the effective-mass model. However, work on a series of doped materials ranging from amorphous to nanocrystalline silicon showed that the Hall voltage recovered its normal sign in low-mobility nanocrystalline materials.[22,68]

The Hall mobilities on polycrystalline CIGS measured by Rusu *et al.*[14] that are illustrated near the bottom of Fig. 1 are low enough that they also seem to be good candidates for the transport-edge perspective. Hall-effect mobilities are measured with currents perpendicular to the growth axis of the thin film and grain boundaries must be involved. Presumably, the effects of the grain boundaries were unimportant compared to those of the disorder within the crystallites for these materials.

VII. BANDTAILS AND URBACH TAILS

We can use the temperature dependence of our drift mobility measurements to constrain the width of a valence bandtail ΔE_V in our materials. Localized bandtail states act as shallow traps, capturing and releasing carriers. The corresponding model is called "multiple trapping,"[20,24,73] which was used to estimate the bandtail widths of Fig. 3. In our application of the model, we use three parameters to fit the drift mobility: the effective-band mobility for holes μ_p^0, the bandtail width ΔE_V, and an emission prefactor frequency ν_0 that characterizes the reemission of holes from a valence bandtail trap back to the valence band.

In Fig. 8 we show temperature-dependent hole drift mobilities for two of our samples along with multiple-trapping calculations; see Appendix D for the details. We have set the prefactor frequency ν_0 to 10^9 s^{-1}, which is at the bottom of the range of values ($\nu_0=1.5\times10^9$ s^{-1} and $\nu_0=10^{12}$ s^{-1}) that have been reported for acceptor levels in CIGS samples with the same $\frac{\text{Ga}}{\text{Ga+In}}$ ratio as ours.[69–72] There have been no estimates of ν_0 for bandtail levels and our measurements do not permit us to make a direct estimate either.

The calculations agree adequately with the measurements at lower temperatures and correspond to bandtail widths of 19 meV (IEC sample) and 12 meV (NREL sample). Both samples show a falloff of the drift mobility for larger temperatures which is inconsistent with the calculation. The calculation neglects any true temperature dependence of the band mobility although some researchers have addressed this effect.[30] Had we used a larger value of ν_0, the fits at low temperature would have been somewhat worse, and the bandtail widths would have been narrower; the band mobility estimates are not much affected by ν_0. We think the calculations are mainly useful for illustrating the band mobility and for setting an upper bound to the bandtail widths. If the multiple-trapping model does apply in CIGS, the drift mobilities should fall substantially at temperatures lower than 77 K, as suggested by extrapolating Fig. 8.

The optical-absorption spectra of CIGS films have Urbach tails that rise exponentially as the photon energy approaches the bandgap of the material; the reported widths of these tails vary from 9–71 meV.[38–44] Urbach tails are a nearly universal aspect of optical absorption in semiconductors. One component of the Urbach tail is the width of the valence bandtail and indeed in amorphous silicon the width of the Urbach tail is often equated with it.[73,74] This component may be considered as a response to static disorder and is essentially a projection of a more complete picture incorporating thermal fluctuations.[75] There are other possible components such as electric field fluctuations due to charged defects that couple to the optical properties through electroabsorption effects.[76]

Wasim *et al.*[41] have reported that epitaxial CIGS crystals can have substantial Urbach tails (greater than 20 meV) associated with copper deficiency in the crystals. From their studies of the temperature-dependent Urbach tails, they proposed that corresponding changes in the vibrational properties of CIGS may lead to the differences in Urbach tails. The effects of such thermal fluctuations on transport measurements sensitive to bandtails does not appear to have been carefully considered.

ACKNOWLEDGMENTS

This research was supported by the National Renewable Energy Laboratory under Contracts No. NDJ-2-30630-24 (Syracuse University) and No. XAT-4-33624-01 (University of Delaware). We thank David Cohen (University of Oregon) for several discussions.

APPENDIX A: ELECTRIC FIELD PROFILE MEASUREMENTS

As noted earlier, our capacitance-voltage measurements deviated from classic "Schottky" behavior (a linear relation between $1/C^2$ vs V); the Schottky form implies an electric field magnitude that falls linearly across the depletion width. For some experimental conditions, we were able to explore

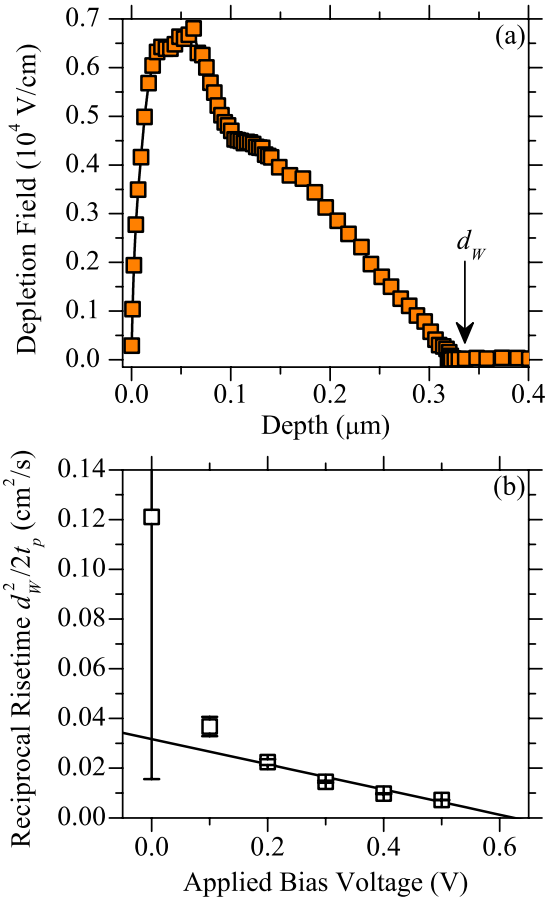

FIG. 9. (Color online) (a) An example of the internal electric field profile as a function of the position for a 0.5 V pulsed bias in a specimen (NREL-1) at $T=293$ K. (b) The corresponding dependence of the normalized, reciprocal transit time $d_W^2/2t_p$ upon applied voltage The slope of the linear fit yields the mobility estimates of 0.035 cm^2/Vs. The voltage intercept (about 0.6 V) is related to the built-in potential V_{BI}.

the form of the electric field profile $E(x)$ in our cells using a photocurrent transient method.[53,77,78] This method is based on the standard TOF experiment. At time $t=0$ the position of the photocarrier charge packet is $x=0$; at later times the packet is at position $x(t)$. Under these conditions, which neglect deep trapping, the photocurrent transient $i(t)$ corresponding to the charge packet Q_0 drifting under the influence of the electric field profile $E(x)$ can be described as follows:

$$E[x(t)] = \frac{i(t)d}{Q_0\mu_D}, \tag{A1}$$

where μ_D is the hole drift mobility and d is the sample thickness. The photocharge $Q(t)$ indicates the position $x(t)$ of the charge packet at time t

$$x(t) = d\frac{Q(t)}{Q_0}, \tag{A2}$$

where $Q(t)$ is the integral of the photocurrent $i(t)$.

In Fig. 9, we present the field profile obtained by applying these equations to the photocurrent transient measurements of sample NREL-1 at +0.5 V; Q_0 was evaluated at −0.5 V. We set $d=d_W(V)$, where d_W is the voltage-dependent depletion width [0.35 μm for Fig. 9(a)] determined from the capacitance measurements. We used $\mu_D=0.035$ cm^2/Vs as obtained from the transit-time analysis presented in Fig. 9(b). The form of the field profile is reasonably linear from 0.05 to 0.3 μm; the behavior for smaller depths is affected by the finite electronic rise time of the system.

The integral V_i of this field is 0.1 V, which can be related to the applied voltage and the built-in field in the cell. The built-in field in the cell was characterized using the voltage intercept $V_0=0.6$ V from Fig. 9(b). V_i should be related to V_0 and the applied voltage ($V=0.5$ V) as $V_0-V=V_i$, which is reasonably consistent with the measurements.

APPENDIX B: EXTENDED HECHT ANALYSIS: TRANSIENT PHOTOCHARGE MEASUREMENTS IN A DEPLETION LAYER WITH DEEP TRAPPING

Transient photocurrents are the response measured in an external biasing circuit following a pulse that creates a sheet of photocarriers, ideally at position $x=0$ and time $t=0$. The photocharge $Q(t)$ obtained by integrating the transient photocurrent $i(t)$ reflects both the position of the photocarrier sheet $x(t)$ and also the loss of photocarriers due to deep trapping. Assuming that the surviving charge of mobile photocarriers at time t is $Q_0\exp(-t/\tau)$, where τ is the deep-trapping time, we can write the following, fairly general equation for $Q(t)$:

$$Q(t) = Q_0\left[\frac{x(t)\exp(-t/\tau)}{d} + \int_0^t \frac{dt'}{\tau}\frac{x(t')\exp(-t'/\tau)}{d}\right], \tag{B1}$$

where Q_0 is the total photocharge generated by the initial light pulse and d is the thickness of the specimen. When the electric field across the specimen is uniform, the sheet of mobile carriers is displaced according to $x(t)=\mu Et$ ($t \le d/\mu E$). In this model, the photocharge does not change after $t=d/\mu E$, when carriers that are not trapped reach the back electrode; we are neglecting the reemission from traps that must ultimately occur to reestablish thermal equilibrium. Evaluating the integral in Eq. (B1) for $t=d/\mu E$ gives

$$Q = \frac{Q_0\tau\mu E}{d}\left[1-\exp\left(-\frac{d}{\tau\mu E}\right)\right], \tag{B2}$$

which is the well-known Hecht equation for the photocharge collection as a function of applied field.[54,55] In addition to Q, we typically measure the risetime t_p at each applied voltage, where t_p is defined as the time to reach 50% of the asymptotic charge. From Eq. (B1) we find the photocharge risetime is

$$t_p = \tau\ln\left[\frac{2}{1+\exp(-t_T/\tau)}\right]. \tag{B3}$$

When the electric field is nonuniform, Eq. (B1) is still valid, but Eqs. (B2) and (B3) must be modified. We consider

the case for a field that declines linearly to zero across a depletion width d_W: $E(x)=E_0(1-x/d_W)$, for which we calculate that the displacement of the sheet is $x(t)=d_W[1-\exp(-\mu t E_0/d_W)]$. We simplify this expression using the definition of a transit time $t_T=\mu_D E_0/d_W$, leading to

$$x(t) = d_W[1 - \exp(-t/t_T)]. \tag{B4}$$

Substituting Eq. (B4) into Eq. (B1) and solving the integral, the resulting photocharge is

$$Q(t) = Q_0 \frac{\tau}{\tau + t_T}\left[1 - \exp\left(-\frac{t}{\tau}\right)\exp\left(-\frac{t}{t_T}\right)\right] \tag{B5}$$

and the asymptotic charge ($t \to \infty$) is

$$Q_\infty = Q_0 \tau/(\tau + t_T). \tag{B6}$$

In terms of the voltage $V_{BI}-V$ across the sample, our definition for t_T is

$$t_T = d_W^2/2\mu_D(V_{BI} - V), \tag{B7}$$

which yields the alternative form for Q_∞

$$Q_\infty = Q_0\left[1 + \frac{d_W^2}{2\mu\tau(V_{BI} - V)}\right]^{-1}. \tag{B8}$$

Additionally, from Eq. (B5) we obtain photocharge risetime

$$\frac{d_W^2}{2t_p} = \frac{\left[\mu_D(V_{BI} - V) + \dfrac{d_W^2}{2\tau}\right]}{\ln(2)}. \tag{B9}$$

We used this expression to obtain the mobility from the photocharge and risetime measurements.

APPENDIX C: EFFECTS OF ELECTRONIC RISETIMES AND LASER PULSEWIDTH ON PHOTOCHARGE RISETIME ESTIMATION

The risetime of the photocharge convolves several different response times: (i) the photocarrier risetime t_p, (ii) the laser pulsewidth t_{laser}, and (iii) the RC response time coming from the product of the depletion-layer capacitance C with the 100 Ohm effective resistance of the electronics (pulser and oscilloscope), and (iv) the dielectric relaxation time of the bottom, undepleted layer of the sample. A rough guide to the effects of (ii), (iii), and (iv) can obtained from the uncorrected photocharge risetime t_R as determined experimentally at large reverse bias (cf. Fig. 5), where photocarrier risetime is shorter than the risetime due to the other effects.

However, because the depletion-layer capacitances of the samples increase as the bias voltage increases, this method is not sufficient to estimate the electronic effects for larger (more positive) bias voltages. We also studied the purely electronic effects (iii) and (iv) explicitly by measuring the risetime $t_{V\text{-}step}$ of the charge response of the sample to the bias voltage step. We calculated photocarrier risetime t_p at the varying voltages using an approximation for convolving risetimes proposed by Walken and Wallman[79]

$$t_p^2 = t_R^2 - t_{laser}^2 - t_{V\text{-}step}^2. \tag{C1}$$

The laser risetime is 3 ns. We checked this expression using the uncorrected photocharge risetime t_R at large reverse-bias voltage, where t_p is small, and found satisfactory agreement.

APPENDIX D: BANDTAIL MULTIPLE-TRAPPING EXPRESSIONS

The fittings in Fig. 8 are based on the low-temperature form for bandtail multiple trapping[24]

$$\mu_D = \left(\frac{L}{E}\nu_0\right)^{1-1/\alpha}(K\mu_p^0)^{1/\alpha}, \quad \alpha < 1, \tag{D1}$$

where: $K \equiv \sin(\pi\alpha)/[\alpha\pi(1-\alpha)]$ and $\alpha \equiv \frac{k_B T}{\Delta E} < 1$ is the dispersion parameter, k_B is the Boltzmann constant, μ_p^0 is the band mobility, ΔE is the bandtail width, and L/F is the ratio of the displacement to the electric field at which the drift mobility is evaluated. We used a simple extrapolation of this expression to accommodate the transition to the high-temperature regime $\alpha > 1$

$$\frac{1}{\mu_D'} = \frac{1}{\mu_p^0} + \frac{1}{\mu_D}. \tag{D2}$$

There have been several papers that treat the transition from the low-temperature to the high-temperature regime of bandtail multiple trapping; see Ref. 24 for further discussion. The present treatment is simpler than these but has the correct behavior at low and high temperatures.

[1] I. Repins, M. A. Contreras, B. Egaas, C. DeHart, J. Scharf, C. L. Perkins, B. To, and R. Noufi, Prog. Photovoltaics. **16**, 235 (2008).

[2] M. A. Green, K. Emery, Y. Hishikawa, and W. Warta, Prog. Photovoltaics. **17**, 85 (2009).

[3] C. H. Champness, Proceedings of the 29th IEEE Photovoltaic Specialists Conference (IEEE, Piscataway, NY, 2002), p. 732.

[4] S. Siebentritt, S. Sadewasser, M. Wimmer, C. Leendertz, T. Eisenbarth, and M. Ch. Lux-Steiner, Phys. Rev. Lett. **97**, 146601 (2006).

[5] Y. Yan, C. S. Jiang, R. Noufi, S. H. Wei, H. R. Moutinho, and M. M. Al-Jassim, Phys. Rev. Lett. **99**, 235504 (2007).

[6] D. J. Schroeder, J. L. Hernandez, G. D. Berry, and A. Rockett, J. Appl. Phys. **83**, 1519 (1998) and references therein.

[7] T. Irie, S. Endo, and S. Kimura, Jpn. J. Appl. Phys. **18**, 1303 (1979).

[8] J. Stankiewicz, W. Giriat, J. Ramos, and P. Vecchi, Sol. Energy Mater. **1**, 369 (1979).

[9] S. M. Wasim, Sol. Cells **16**, 289 (1986).

[10] H. Neumann and R. D. Tomlinson, Sol. Cells **28**, 301 (1990).

[11] B. Schumann, H. Neumann, A. Temple, G. Kűhn, and E. Nowak, Krist. Tech. **15**, 71 (1980).

[12] S. Schuler, S. Nishiwaki, J. Beckmann, N. Rega, S. Brehme, S. Siebentritt, and M. C. Lux-Steiner, in Proceedings of the 29th IEEE Photovoltaic Specialists Conference, edited by J. Benner, (IEEE, New Orleans, 2002), pp. 504–507.
[13] I. L. Repins, B. J. Stanbery, D. L. Young, S. S. Li, W. K. Metzger, C. L. Perkins, W. N. Shafarman, M. E. Beck, L. Chen, V. K. Kapur, D. Tarrant, M. D. Gonzalez, D. G. Jensen, T. J. Anderson, X. Wang, L. L. Kerr, B. Keyes, S. Asher, A. Delahoy, and B. Von Roedern, Prog. Photovoltaics. **14**, 25 (2006).
[14] M. Rusu, P. Gashin, and A. Simashkevich, Sol. Energy Mater. Sol. Cells **70**, 175 (2001).
[15] M. Nishitani, T. Negami, N. Kohara, and T. Wada, J. Appl. Phys. **82**, 3572 (1997).
[16] Y. Tang, R. Braunstein, and B. von Roedern, Appl. Phys. Lett. **63**, 2393 (1993).
[17] Th. Meyer, F. Engelhardt, J. Parisi, and U. Rau, J. Appl. Phys. **91**, 5093 (2002).
[18] N. A. K. Abdul-Hussein, A. N. Y. Samaan, K. D. Tomlinson, A. E. Hill, and H. Neumann, Cryst. Res. Technol. **20**, 509 (1985).
[19] R. Kaigawa, A. Ohyama, T. Wada, and R. Klenk, Phys. Status Solidi C **3**, 2568 (2006).
[20] T. Tiedje, in *The Physics of Hydrogenated Amorphous Silicon*, edited by J. D. Joannopoulos and G. Lucovsky (Springer-Verlag, Berlin, 1984), Vol. 2, pp. 261–300.
[21] J. Y. W. Seto, J. Appl. Phys. **46**, 5247 (1975).
[22] W. E. Spear and P. G. LeComber, in *The Physics of Hydrogenated Amorphous Silicon: Structure, Preparation, and Devices*, edited by J. D. Joannopoulos and G. Lucovsky (Springer-Verlag, Berlin, 1984), Vol. 1, pp. 63–118.
[23] N. F. Mott, *Conduction in Non-Crystalline Materials*, 2nd ed. (Oxford University Press, Oxford, 1993).
[24] E. A. Schiff, J. Phys.: Condens. Matter **16**, S5265 (2004).
[25] K. Seeger, *Semiconductor Physics: An Introduction*, 9th ed. (Springer-Verlag, Berlin, New York, 2004), pp. 159–221.
[26] H. Neumann, E. Nowak, and G. Kűhn, Cryst. Res. Technol. **16**, 1369 (1981).
[27] H. Neumann, Sol. Cells **16**, 317 (1986).
[28] S. Siebentritt, Thin Solid Films **480-481**, 312 (2005).
[29] R. I. Devlen, J. Tauc, and E. A. Schiff, J. Non-Cryst. Solids **114**, 567 (1989).
[30] G. Juska, K. Arlauskas, J. Kocka, M. Hoheisel, and P. Chabloz, Phys. Rev. Lett. **75**, 2984 (1995).
[31] Y. Yan, R. Noufi, K. M. Jones, K. Ramanathan, M. M. Al-Jassim, and B. J. Stanbery, Appl. Phys. Lett. **87**, 121904 (2005).
[32] S. R. Kurtz, A. A. Allerman, C. H. Seager, R. M. Sieg, and E. D. Jones, Appl. Phys. Lett. **77**, 400 (2000).
[33] H. W. Schock and U. Rau, Physica B **308-310**, 1081 (2001).
[34] G. Horowitz, R. Hajlaoui, and P. Delannoy, J. Phys. III **5**, 355 (1995).
[35] A. Salleo, T. W. Chen, A. R. Völkel, Y. Wu, P. Liu, B. S. Ong, and R. A. Street, Phys. Rev. B **70**, 115311 (2004).
[36] A. R. Völkel, R. A. Street, and D. Knipp, Phys. Rev. B **66**, 195336 (2002).
[37] R. A. Street, S. E. Ready, F. Lemmi, K. S. Shah, P. Bennett, and Y. Dmitriyev, J. Appl. Phys. **86**, 2660 (1999).
[38] J. D. Cohen, J. T. Heath, and W. N. Shafarman, in *Wide-Gap Chalcopyrites*, Springer Series in Materials Science, edited by S. Siebentritt and U. Rau (Springer, New York, 2006), pp. 69–90.
[39] P. T. Erslev, J. W. Lee, W. N. Shafarman, and J. D. Cohen, Thin Solid Films **517**, 2277 (2009).
[40] A. Meeder, D. Fuertes Marron, A. Rumberg, M. Ch. Lux-Steiner, V. Chu, and J. P. Conde, J. Appl. Phys. **92**, 3016 (2002).
[41] S. M. Wasim, C. Rincon, G. Marin, P. Bocaranda, E. Hernandez, I. Bonalde, and E. Medina, Phys. Rev. B **64**, 195101 (2001).
[42] T. Shioda, S. Chichibu, T. Irie, H. Nakanishi, and T. Kariya, J. Appl. Phys. **80**, 1106 (1996).
[43] G. A. Medvedkin, Yu. V. Rud, and M. A. Tairov, Phys. Status Solidi B **144**, 809 (1987).
[44] H. Nakanishi, T. Sawaya, S. Endo, and T. Irie, Jpn. J. Appl. Phys., Suppl. **32-3**, 200 (1993).
[45] M. A. Contreras, B. Egaas, K. Ramanathan, J. Hiltner, A. Swartzlander, F. Hasoon, and R. Noufi, Prog. Photovoltaics. **7**, 311 (1999).
[46] W. N. Shafarman, R. Klenk, and B. E. McCandless, J. Appl. Phys. **79**, 7324 (1996).
[47] W. N. Shafarman and J. Zhu, in *II–VI Compound Semiconductor Photovoltaic Materials*, MRS Symposia Proceedings No. 688, edited by R. Noufi, R. W. Birkmire, D. Lincot, and H. W. Schock (Materials Research Society, Pittsburgh, PA, 2001), p. H2.3.1.
[48] S. M. Sze, in *Physics of Semiconductor Devices*, 1st ed. (Wiley, New York, 1969), p. 9.
[49] Since the direction of the applied electric filed is parallel with the *c* axis, we concluded that our estimate of the dielectric constant was determined parallel with the *c* axis.
[50] M. I. Alonso, M. Garriga, C. A. Durante Rinćon, E. Hernández, and M. León, Appl. Phys. A: Mater. Sci. Process. **74**, 659 (2002).
[51] S. H. Han, A. M. Hermann, F. S. Hasoon, H. A. Al-Thani, and D. H. Levi, Appl. Phys. Lett. **85**, 576 (2004).
[52] R. A. Street, Appl. Phys. Lett. **41**, 1060 (1982).
[53] R. A. Street, Phys. Rev. B **27**, 4924 (1983).
[54] K. Hecht, Z. Phys. **77**, 235 (1932).
[55] W. E. Spear and J. Mort, Proc. Phys. Soc. London **81**, 130 (1963).
[56] S. Fonash, *Solar Cell Device Physics* (Wiley, New York, 1982), p. 181.
[57] I. Balberg, D. Albin, and R. Noufi, Appl. Phys. Lett. **54**, 1244 (1989).
[58] J. W. Lee, J. D. Cohen, and W. N. Shafarman, Thin Solid Films **480-481**, 336 (2005). The admittance mobilities are based on measurements of the frequency-dependent impedance of diode structures. In brief, frequency-dependent measurements yielded the dielectric relaxation time τ dielectric of the bottommost, undepleted region of the CIGS thin films. The estimates of admittance mobilities correspond to cases in which the impedance measurements could be interpreted in terms of a well-defined density of mobile holes; knowledge of both p and τ dielectric yields the admittance mobility from standard expressions for τ dielectric.
[59] S. Siebentritt and S. Schuler, J. Phys. Chem. Solids **64**, 1621 (2003).
[60] F. Reif, *Fundamentals of Statistical and Thermal Physics* (McGraw-Hill, San Francisco, 1965), p. 485.
[61] H. Overhof and W. Beyer, Philos. Mag. B **43**, 433 (1981).
[62] H. Overhof and P. Thomas, *Electronic Transport in Hydrogenated Amorphous Semiconductors* (Springer-Verlag, Berlin, New York, 1989).
[63] M. Silver, G. Schoenherr, and H. Baessler, Phys. Rev. Lett. **48**,

352 (1982).
[64] D. Monroe, Phys. Rev. Lett. **54**, 146 (1985).
[65] S. D. Baranovskii, I. P. Zvyagin, H. Cordes, S. Yamasaki, and P. Thomas, J. Non-Cryst. Solids **299-302**, 416 (2002).
[66] T. Dylla, F. Finger, and E. A. Schiff, Appl. Phys. Lett. **87**, 032103 (2005).
[67] T. Dylla, S. Reynolds, R. Carius, and F. Finger, J. Non-Cryst. Solids **352**, 1093 (2006).
[68] W. E. Spear, G. Willeke, P. G. LeComber, and A. G. Fitzgerald, J. Phys. Colloq. **42**, C4–257 (1981).
[69] JinWoo Lee, Ph.D. thesis, University of Oregon, 2008.
[70] R. Herberholz, T. Walter, C. Müller, T. Friedlmeier, H. W. Shock, M. Saad, M. Ch. Lux-Steiner, and V. Alberts, Appl. Phys. Lett. **69**, 2888 (1996).
[71] V. Mertens, J. Parisi, and R. Reineke-Koch, J. Appl. Phys. **101**, 104507 (2007).
[72] T. Walter, R. Herberholz, C. Müller, and H. W. Schock, J. Appl. Phys. **80**, 4411 (1996).
[73] T. Tiedje, B. Abeles, and J. M. Cebulka, Solid State Commun. **47**, 493 (1983).
[74] J. A. Howard and R. A. Street, Phys. Rev. B **44**, 7935 (1991).
[75] C. H. Grein and S. John, Phys. Rev. B **41**, 7641 (1990).
[76] J. D. Dow and D. Redfield, Phys. Rev. B **5**, 594 (1972).
[77] R. Könenkamp, S. Muramatsu, H. Itoh, S. Matsubara, and T. Shimada, Appl. Phys. Lett. **57**, 478 (1990).
[78] R. Vanderhaghen and C. Longeaud, in *Amorphous Silicon Technology*, MRS Symposia Proceedings No. 149, edited by A. Madan, M. J. Thompson, P. C. Taylor, Y. Hamakawa, and P. G. LeComber (Material Research Society, Pittsburgh, PA, 1989), pp. 357–363.
[79] R. Walker and H. Wallman, *Vacuum Tube Amplifiers*, 4th ed. (McGraw-Hill, Columbus, 1948), p. 77.